



Article

Lithium-Rich Pegmatite Detection Integrating High-Resolution and Hyperspectral Satellite Data in Zhawulong Area, Western Sichuan, China

Wenqing Ding ^{1,2} , Lin Ding ^{1,2,*}, Qingting Li ³ , Jinxiang Li ¹ and Liyun Zhang ¹

¹ State Key Laboratory of Tibetan Plateau Earth System, Environment and Resources, Institute of Tibetan Plateau Research, Chinese Academy of Sciences, Beijing 100101, China

² University of Chinese Academy of Sciences, Beijing 100049, China

³ Aerospace Information Research Institute, Chinese Academy of Sciences, Beijing 100094, China

* Correspondence: dinglin@itpcas.ac.cn; Tel.: +86-010-840-97-104

Abstract: Lithium (Li) has grown to be a strategic key metal due to the enormous demand for the development of new energy industries over the world. As one of the most significant sources of Li resources, pegmatite-type Li deposits hold a large share of the mining market. In recent years, several large and super-large spodumene (Spd)-rich pegmatite deposits have been discovered successively in the Hoh-Xil–Songpan–Garzê (HXSG) orogenic belt of the northern Tibetan Plateau, indicative of the great Li prospecting potential of this belt. Hyperspectral remote sensing (HRS), as a rapidly developing exploration technology, is especially sensitive to the identification of alteration minerals, and has made important breakthroughs in porphyry copper deposit exploration. However, due to the small width of the pegmatite dykes and the lack of typical alteration zones, the ability of HRS in the exploration of Li-rich pegmatite deposits remains to be explored. In this study, Li-rich pegmatite anomalies were directly extracted from ZY1-02D hyperspectral imagery in the Zhawulong (ZWL) area of western Sichuan, China, using target detection techniques including Adaptive Cosine Estimator (ACE), Constrained Energy Minimization (CEM), Spectral Angle Mapper (SAM), and SAM with BandMax (SAMBMax). Further, the Li-rich anomalies were superimposed with the distribution of pegmatite dykes delineated based on GF-2 high-resolution imagery. Our final results accurately identified the known range of Spd pegmatite dykes and further predicted two new exploration target areas. The approaches used in this study could be easily extended to other potential mineralization areas to discover new rare metal pegmatite deposits on the Tibetan Plateau.

Keywords: pegmatite; lithium; mineral exploration; ZY1-02D; hyperspectral remote sensing; target detection; Tibetan Plateau



Citation: Ding, W.; Ding, L.; Li, Q.; Li, J.; Zhang, L. Lithium-Rich Pegmatite Detection Integrating High-Resolution and Hyperspectral Satellite Data in Zhawulong Area, Western Sichuan, China. *Remote Sens.* **2023**, *15*, 3969. <https://doi.org/10.3390/rs15163969>

Academic Editors: Ana Cláudia Teodoro, Joana Cardoso-Fernandes and Alexandre Lima

Received: 11 July 2023

Revised: 9 August 2023

Accepted: 9 August 2023

Published: 10 August 2023



Copyright: © 2023 by the authors. Licensee MDPI, Basel, Switzerland. This article is an open access article distributed under the terms and conditions of the Creative Commons Attribution (CC BY) license (<https://creativecommons.org/licenses/by/4.0/>).

1. Introduction

Lithium (Li), the lightest metal element in nature, is widely used in various industries such as air treatment, ceramics, glass, aeronautics, pharmaceuticals, and polymers [1]. In particular, it is known as “white oil” due to its application in rechargeable Li-ion batteries, serving as a substitute for fossil fuels to power burgeoning electric vehicles. Sovacool et al. [2] estimated that the annual demand for Li in the field of low-carbon energy technology alone will reach 415,000 tons by 2050. Therefore, Li is crucial to the development of a low-carbon future and the mitigation of global warming [3], and has been listed as one of the most critical metals in many countries over the world [2,4,5]. Present Li deposit worldwide could be classified as three types—brine, hard rock, and clay. Particularly, hard rock-type Li deposit holds a significant market share due to its simplicity of mining and short investment cycle [3]. As the primary source of hard rock type Li ores, spodumene (Spd, $\text{LiAlSi}_2\text{O}_6$) pegmatite has become one of the most valuable mineral resources nowadays with high Li content and high rate of extraction [3,6].

The Tibetan Plateau contains abundant Li resources preserved in salt-lake brine and granitic pegmatites [7]. The pegmatite-type Li deposits are mainly distributed in the Himalayan orogenic belt in the south [8] and the Hoh-Xil–Songpan–Garzê–West Kunlun orogenic belt in the north [7,9]. However, these metallogenic belts are generally high-elevations, cold, hypoxic with harsh environmental conditions, raising great difficulties during field investigation. Therefore, it is necessary to develop a more efficient and cost-effective exploration method specifically for Spd-rich pegmatite deposits. The rapid development of remote sensing technology has made it possible [10–12]. There have been several preliminary attempts to detect Li mineralization through remote sensing techniques mainly in Portugal/Spain [13–17], China [18–26], Afghanistan [27], Mozambique [28,29], Namibia [30–33], and Brazil [34]. These studies aimed at mapping the associated altered zones (i.e., iron oxides and clay minerals) or directly identifying Li-bearing minerals (e.g., spodumene, lepidolite, petalite, and cookeite) to locate the distribution of mineralized areas. Besides, optical and radar sensors were also used for interpreting lineaments and circular structures that may control pegmatite emplacement to assist in predicting mineralized areas [18,24,35]. The optical satellite data commonly used at present include Landsat-5, Landsat-8, ASTER, Sentinel-2 with medium spatial resolution, and Worldview-2, Worldview-3, RapidEye, Geoeye-1 with high spatial resolution. Cardoso-Fernandes et al. [14] carried out the representative work in the Fregeneda–Almendra (Spain-Portugal) aplite-pegmatite field. Based on different multispectral spaceborne platforms with a medium resolution, several classic methods, including false color composite, band ratio, and selective principal component analysis, have been adapted to successfully identify the known Li-bearing pegmatite open-pit mines [14]. In recent research, machine learning-based classifiers were widely used for various ore deposit exploration including Li [36]. For example, Köhler et al. [16] proved the application of artificial neural networks in delineating exploration targets of Li-rich potential areas from Central Portugal. Additionally, support vector machine models were trained on Sentinel-2 images to map the distribution of Li-bearing pegmatites in the Fregeneda–Almendra region [15].

The enhancement of spectral resolution in sensors significantly improves satellites' capability to identify specific ground objects [37]. In recent years, hyperspectral remote sensing (HRS) has gained widespread utilization in geological mapping and mineral exploration [38,39], particularly in the exploration of porphyry copper deposits and epithermal gold deposits [40]. This is primarily due to the prevalence of extensive mineral alteration zones in such deposits, which exhibit distinct spectral characteristics [39]. In contrast, pegmatite deposits are typically characterized by their small outcrop area and lack of prominent regional alteration features, making it challenging to apply established HRS exploration models. Therefore, the direct detection of Li-bearing pegmatites using hyperspectral data remains a subject that requires verification, particularly considering that the width of most pegmatite dykes is often smaller than the spaceborne sensor's spatial resolution. In the Namibia, Oshigami et al. [33] applied the airborne HyMap hyperspectral data with a 5 m resolution to delineate the distribution of lepidolite, and Booyesen et al. [31] mapped cookeite and montebasite at outcrop scale using ground-based hyperspectral imaging, whereas, there are few cases of applying satellite hyperspectral imagery to target Li deposits so far [25,26], mainly due to its low spatial resolution and limited data source.

The limited number of bands poses a challenge for extracting Li-bearing pegmatites based on multispectral remote sensing, resulting in high uncertainty of results and a certain number of false anomalies. While HRS has found extensive application in mapping alteration zones, its potential for exploring pegmatite-type rare metal deposits is yet to be fully explored. This study directly extracted Li-rich pegmatite anomalies from ZY1-02D hyperspectral imagery in the Zhawulong (ZWL) deposit area of western Sichuan, China, using several target detection techniques. Meanwhile, the spatial distribution of the pegmatite dykes was directly delineated based on GF-2 satellite image with high spatial resolution. Further, the Li-rich anomalies were superimposed with the distribution of pegmatites to predict the potential Li-mineralized target areas. The methodology proposed

in this study enables direct detection of the distribution of Li-rich pegmatites, reducing the interference of false anomalies. It holds certain implications for exploring rare metal (i.e., Li and Be) deposits in remote and undiscovered areas.

2. Study Area and Geological Setting

The Hoh-Xil–Songpan-Garzê (HXSG) orogenic belt, situated in the northern Tibetan Plateau and sandwiched between the South China block to the east, the Kunlun terrane to the north, and the Qiangtang terrane to the south (Figure 1a), is the most important and promising metallogenic belt of rare metals in China. This belt is mainly composed of thick (5–15 km) Triassic turbidites of Bayan Har Mountain Group which are considered as the marine sediments of a “remnant” ocean [41], “Mediterranean-style” basin [42], or “back-arc basin” [43]. The Triassic turbidites were extensively intruded by Late Triassic–Early Jurassic granitoids [44], usually forming shales and slates rich in cordierite or andalusite in their contact metamorphic zones. Particularly in the easternmost of the HXSG belt, a series of dome structures were developed due to the dynamic intrusion of the pluton, which could create favorable conditions for the rare metal mineralization of pegmatite [45,46]. Around these domes, a number of large and super-large rare metal deposits have been discovered (Figure 1a), including Jiajika (JJK), Ke’eryin (KEY), Xuebaoding (XBD), and Zhawulong (ZWL), and their ore-forming ages are accordantly concentrated in the Late Triassic to Early Jurassic [47,48].

The ZWL spodumene pegmatite deposit is geographically located at the junction of Shiqu County in Sichuan Province and Chindu County in Qinghai Province and geologically lies in the eastern HXSG orogenic belt [49,50]. In this region, the Late Triassic muscovite granite pluton intruded in Triassic metasedimentary strata, forming a dome structure (Figure 1b). The dome is conducive to the formation of Li-Cs-Ta pegmatite and the enrichment of Li group elements [45], and the ore dykes are exposed in the contact zone between granitic pluton and wall rock of turbidites in research area. Exposed strata in the ore field are mainly composed of Triassic metasediments and Quaternary sediments [49–52]. The Triassic lithologies include biotite quartz schist, phyllite, biotite granulite, metamorphic sandstone, and metamorphic shale. The Quaternary is mainly sand and gravel alluvium, accounting for more than 50% of this area, and is widely covered by meadows in summer. The granitic pluton is emplaced into anticlinal core composed of turbidites including sandstone and siltstone, occurring as an irregular fusiform on the surface, and its mineral composition mainly includes quartz, feldspar, and muscovite. The residual roof of wall rock still remains at the top of the granitic intrusion, indicating a low degree of regional denudation. It is speculated that there may be undiscovered ore bodies that have not yet been exposed in the deep [49]. Pegmatites in the ore field are dominated by microcline pegmatite, microcline-albite pegmatite, and albite-spodumene pegmatite [49–52]. As the ore-forming dykes, albite-spodumene pegmatites intruded the Triassic strata on the south side of the granitic pluton, outcropping as a linear structure, and are composed of large crystals of quartz, albite, spodumene, and muscovite. Spodumene is primarily grayish white and light green, and it typically appears as semi-euhedral to euhedral plate columnar crystal and is generally thick and big without specific alteration (Figure 2). The Li-rich pegmatite dyke occurs with a length of more than 1000 m and a width of 5 m on the ground surface. The Li₂O reserves are approximately 100,000 tons with an average Li₂O grade of 1.2%, indicating a large-scale Li deposit [49]. According to the geophysical survey results, the ore dyke can extend further into the deep and laterally, and the prospective resources of Li₂O were estimated to exceed 700,000 tons [50,53], indicative of tremendous exploration potential. Recently, new Spd-rich pegmatites have been successively discovered in Caolong [54,55] and Gaduo [56] areas, approximately 8–70 km far from the western ZWL deposit, suggesting that there are still undiscovered deposits in the vicinity of the ore field. However, this region belongs to the Sanjiangyuan National Nature Reserve, and the remote terrain and limited accessibility make it difficult to conduct large-scale geological and geophysical survey. Remote sensing, as a rapid, non-destructive, and environmentally

friendly technique, can play a crucial role in the exploration of rare metal minerals in this area.

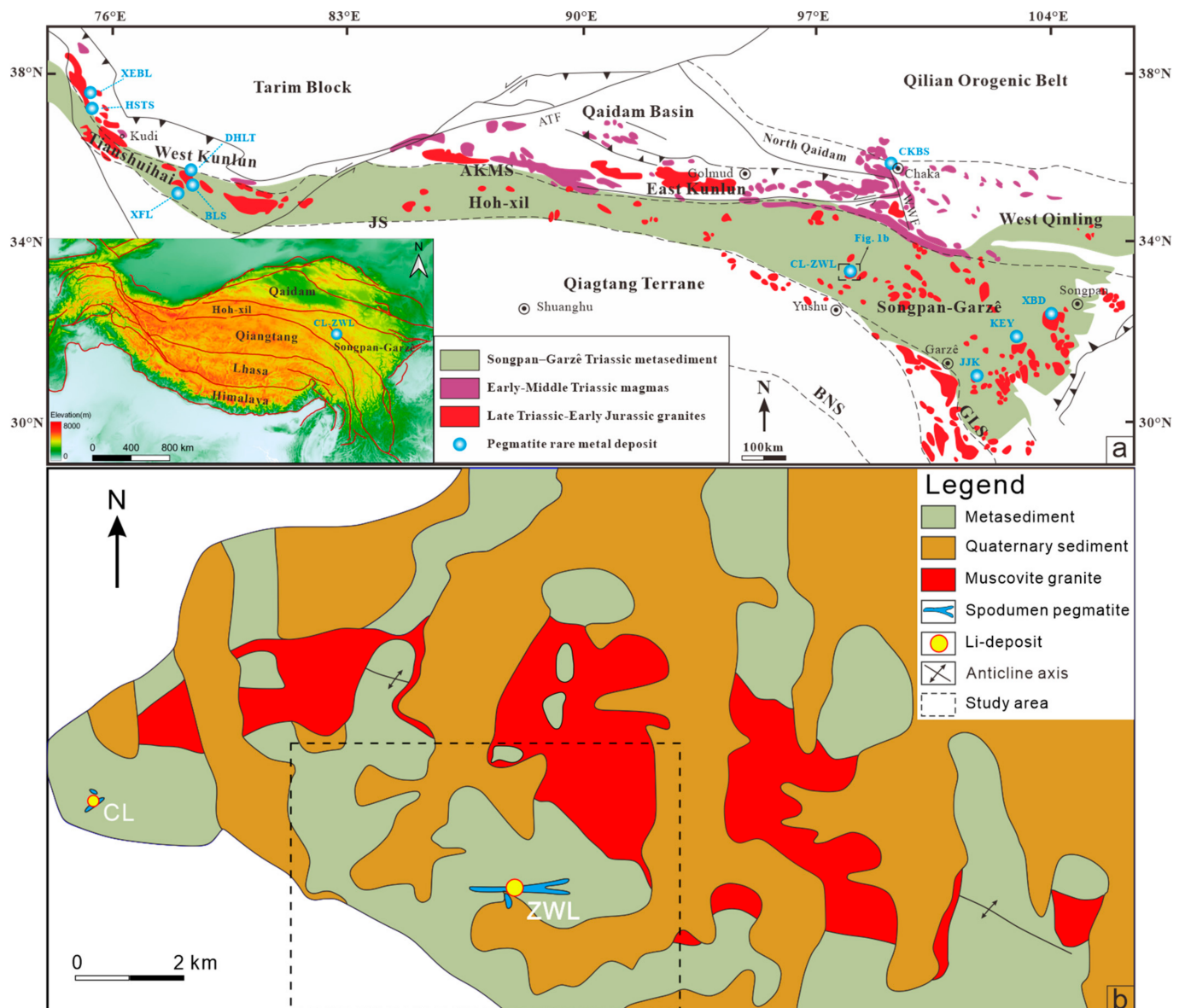


Figure 1. (a) Simplified tectonic map of the major pegmatite rare metal deposits in the Hoh-Xil-Songpan-Garzê-West Kunlun orogenic belt, modified after [48,57]. AKMS: Ayimaqin-Kunlun-Matztagh Suture, JS: Jinshajiang Suture, BNS: Bangong-Nujiang Suture, GLS: Garzê-Litang Suture, CL: Caolong, ZWL: Zhawulong, JJK: Jiajika, KEY: Ke'eryin, XBD: Xuebaoding, CKBS: Chakabeishan, XFL: Xuefengling, BLS: Bailongshan, DHLT: Dahongliutan, HSTS: Huoshitashi, and XEBL: Xiaoberbulong. (b) Simplified geological map of the ZWL ore field after [49].



Figure 2. (a) Field outcrop of spodumene pegmatite in the Zhawulong deposit; (b,c) field pictures of spodumene (Spd) crystals.

3. Materials and Methods

The raw data used in this study mainly include one scene of GF-2 multispectral sensor with a high spatial resolution, and one scene of Advanced Hyperspectral Imager (AHSI) onboard ZY1-02D satellite with a high spectral resolution. The procedures of data pre-processing and image analysis were performed using Environment for Visualizing Images (ENVI) software version 5.3.1 and ArcMap software version 10.8. Figure 3 shows the overall workflow.

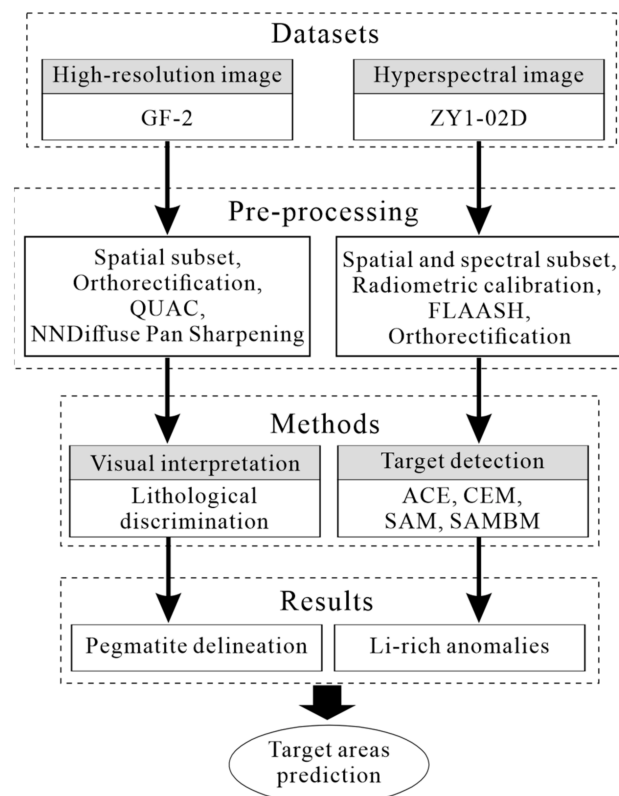


Figure 3. Schematic diagram of overall workflow.

3.1. Data Pre-Processing

3.1.1. GF-2 Satellite

The GF-2 satellite was launched in China on 19 August 2014, with an optimal spatial resolution of better than 1 m, marking the beginning of the “high-resolution era” for China’s civilian remote sensing satellites at the sub-meter level. Its imaging system consisted of

the panchromatic (PAN) camera with a 1 m resolution and the multispectral camera with a 4 m resolution (Table 1). The multispectral camera was configured with 4 bands, covering the spectral range of 0.45–0.89 μm , and the swath width of 45 km was achieved by combining two cameras [58]. The high spatial resolution of the GF-2 satellite provides specific advantages in the geological application, such as the information extraction of structures, strata, and dikes [59–61].

Table 1. GF-2 and ZY1-02D AHSI sensors parameters.

Data	Spectral Range	Spectral Resolution	Pixel Size	Swath Width
GF-2	PAN	0.45–0.90 μm	1 m	
	Blue	0.45–0.52 μm		
	Green	0.52–0.59 μm		45 km
	Red	0.63–0.69 μm		
	NIR	0.77–0.89 μm		
ZY1-02D	VNIR	395–1040 nm	30 m	60 km
	SWIR	1005–2510 nm	20 nm	

The imagery was a level-1A product with radiometric correction, which was imaged on 2 September 2020 and acquired on 8 November 2022 through applying to Natural Resources Satellite Remote Sensing Cloud Service Platform of China (<http://sasclouds.com/english/normal/>, accessed on 8 August 2023). According to the application requirements, the imagery was processed by spatial subset, orthorectification, and quick atmospheric correction (QUAC). Then, the NNDiffuse Pan Sharpening method [62] was employed to fuse the multispectral data with the PAN image to improve its spatial resolution to 1 m while preserving the fidelity of its spectrum (Figure 4). Further, geographical registration between the GF-2 image and ZY1-02D image was performed.

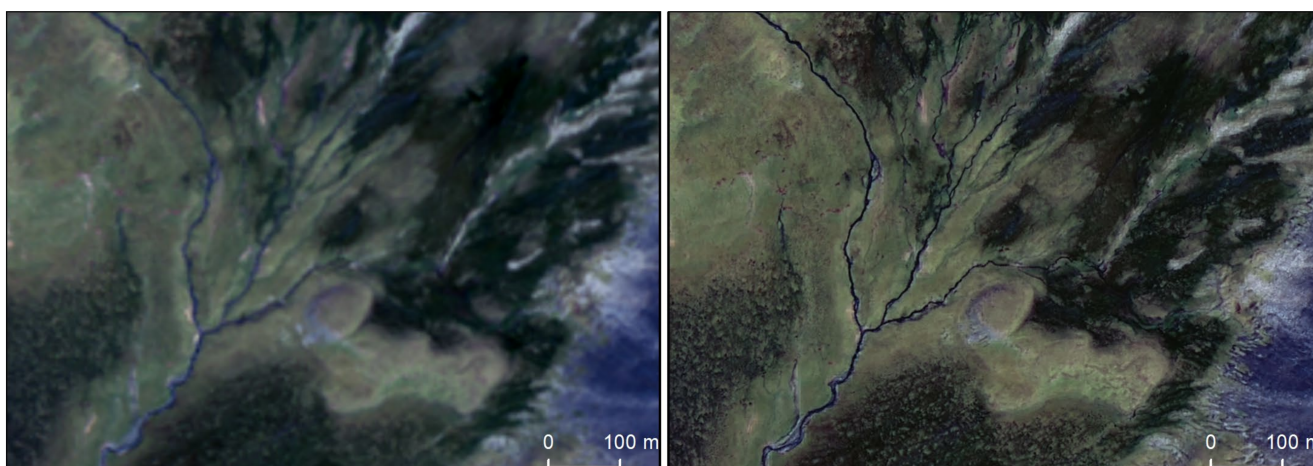


Figure 4. Comparison of image spatial features before (left) and after (right) panchromatic fusion.

3.1.2. ZY1-02D Satellite

The ZY1-02D satellite was launched in China on 12 September 2019, carrying an AHSI, which is the first civilian hyperspectral satellite independently constructed and operated by China. The satellite data can be queried and downloaded from Natural Resources Satellite Remote Sensing Cloud Service Platform of China (<http://sasclouds.com/english/normal/>, accessed on 8 August 2023). As shown in Table 1 [63,64], the ZY1-02D AHSI covers a spectral range of 0.4–2.5 μm equipped with 166 bands. The spectral resolution is 10 nm in the visible and near-infrared (VNIR) region and 20 nm in the shortwave infrared (SWIR) region, and the spatial resolution is 30 m. The ZY1-02D AHSI stands out from existing satellite hyperspectral sensors worldwide due to its superior swath

width of 60 km and signal-to-noise ratio ($\text{SNR} \geq 240@0.4\text{--}0.9 \mu\text{m}$, $\geq 180@0.9\text{--}1.75 \mu\text{m}$, and $\geq 120@1.75\text{--}2.5 \mu\text{m}$) [64]. This makes it highly promising for applications in natural resources survey and mineral information extraction [65–69].

The level-1A imagery used here was imaged on 14 October 2021 and acquired on 22 August 2022. The pre-processing of hyperspectral data mainly includes the following steps:

- (1) Spatial subset to research area and removal of overlapping, water vapor, strip and noise-evident bands (i.e., B1-B2, B77-B79, B96-B102, B124-B133, B164-B166). The remaining 141 bands were used for subsequent analysis;
- (2) Conversion of digital number (DN) value to radiance through radiometric calibration;
- (3) Correction of radiance data to reflectance by using the FLAASH module in ENVI;
- (4) Orthorectification using a Landsat-8 scene as a reference image by “RPC Orthorectification Using Reference Image” tool in ENVI;
- (5) Geographical registration with the GF-2 image. The spatial registration accuracy ($\text{RMSE} < 1$) has been visually verified to meet the requirements of the research.

3.2. Methods

For mineral exploration purpose, remote sensing detection only requires distinguishing whether an object is mineralized, with no necessity for a completed classification of all lithological units. Additionally, ore-bearing pegmatite dykes typically have limited distributions and small areas, appearing as low probability and sub-pixel targets in hyperspectral imagery [70], making it challenging for conventional supervised classification methods to accurately extract such weak anomalies. Considering the mentioned conditions, four target detection techniques based on ZY1-02D hyperspectral data were implemented to directly extract Li-rich pegmatite anomalies in the region.

3.2.1. Constrained Energy Minimization (CEM)

CEM is proposed based on a spectral linear mixing model [71], which assumes that the spectral signal of a mixed pixel is composed of endmembers' spectra weighted by their proportions. It aims to maximize the response of a target signature on a pixel-by-pixel basis while suppressing the response of undesired background signatures, resulting in an optimal estimate of the abundance or fraction of the material of interest in each pixel. Basically, CEM operator employs a finite impulse response (FIR) filter to achieve target detection, which is defined by two constraints [71,72]. The first constraint is to minimize the total output energy of all pixels. The second constraint is to assume the energy of an individual pixel summed across the wavelength range to be 1 when applied to a target spectrum. CEM technique is powerful to deal with a variety of spectral backgrounds, and no a priori knowledge except the desired target signature (either image or laboratory spectra) is required. In previous research, CEM has been successfully applied in various geological fields, such as mine contamination survey [71], lithology mapping [72], and extraction of alteration minerals [73]. In this study, the CEM detector based on minimum noise fraction (MNF) [74,75] was employed to detect Li-rich pegmatite anomalies.

3.2.2. Adaptive Cosine Estimator (ACE)

The ACE algorithm initially assumes that the target and background follow distinct probability models and then utilizes the generalized likelihood ratio (GLR) method to construct a detector [70,76]. It maintains invariance to the relative scaling of input spectra and exhibits a constant false alarm rate (CFAR) in relation to this scaling. ACE uses an angular threshold between the target pixel and the test pixel in a whitening space, which is different from the distance threshold used by the adaptive matched filter (AMF) detector [76]. The same as CEM, ACE does not require knowledge of all the endmembers but the target spectra within an image scene. ACE is not constrained by the size of targets and remains reliable for both small and large targets detection. It has been utilized to extract hydrothermal alterations related to ore deposits [77,78].

3.2.3. Spectral Angle Mapper (SAM)

The SAM is a tool that permits rapid evaluation of the spectral similarity between image spectra and reference spectra and is also the most used technique in geological mapping [79]. The reference spectra can be obtained from either laboratory or field measurements or extracted directly from the image. The algorithm determines the spectral similarity between two spectra by calculating the “angle” between the two spectra, treating them as vectors in a high-dimensional space with dimensionality equal to the number of bands. Smaller spectral angles correspond to higher similarity, and these pixels would be sieved as desired targets. The spectral angle (θ) between a test spectrum t and a reference spectrum r can be calculated by applying the following equation:

$$\theta = \cos^{-1} \left(\frac{\vec{t} \cdot \vec{r}}{|\vec{t}| \cdot |\vec{r}|} \right) \quad (1)$$

3.2.4. Spectral Angle Mapper with BandMax (SAMBM)

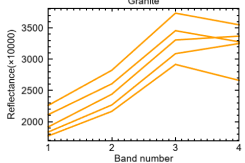
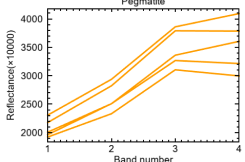
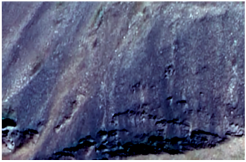
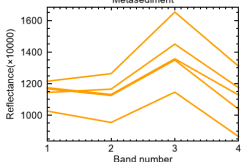
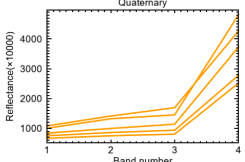
The SAMBM is a target detection method combining SAM and BandMax techniques and can be implemented through the “SAM Target Finder with BandMax” module in ENVI software (<https://www.nv5geospatialsoftware.com/docs/SAMTargetFinderWithBandMax.html>, accessed on 8 August 2023). BandMax is a patented technique developed by Galileo Group, Inc [80]. According to the theory of BandMax, a spectral feature can be defined as any pair of bands that present a unique slope between them. That means it is no longer confined to having only one feature in each band. Then, the number of total features comes to $((n^2) - n)/2$, where n = number of spectral bands. If two very similar mineral spectra were in a data set of their natural environment, more distinguishing features would be found by the BandMax algorithm than standard processing methods. Furthermore, through the real-time interactive threshold adjustment, analysts can narrow down spectral subsets to only key bands with the most vital information [81,82]. This information can help to eliminate redundant identical features between two very similar objects, it allows standard algorithms to give weight to the important, yet subtle, differences between target and background spectra, resulting in reduced false alarms. In this study, the Li-rich pegmatite spectrum was taken as the target, while the granite spectrum was taken as background. The SAMBM was applied to detect targets based on MNF-transformed ZY1-02D hyperspectral data.

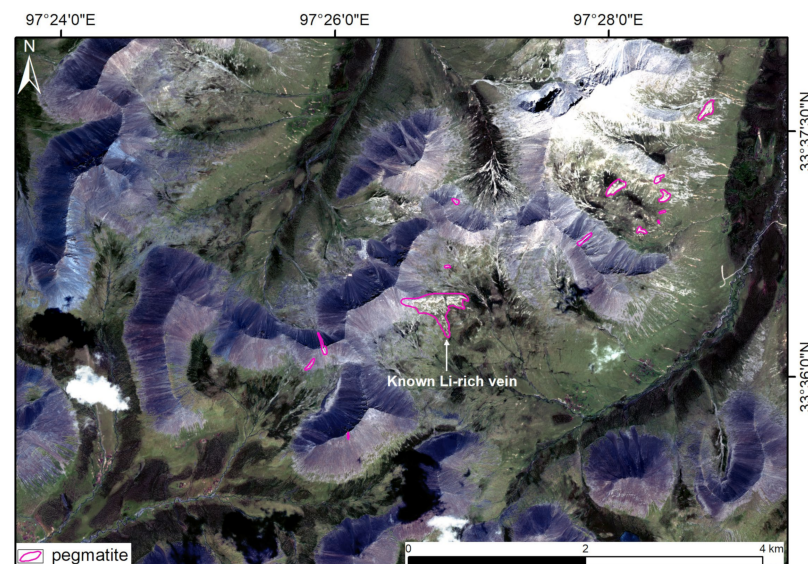
4. Results

4.1. Pegmatite Delineation

Pegmatite is commonly outcropped in a small width and area, making the spatial resolution of satellite imagery a decisive role in the accuracy and efficiency of pegmatite dykes delineation. GF-2 multispectral sensor has a resolution of 4 m, and it generates color image with a resolution of 1 m after fusion with the panchromatic image, containing abundant spatial texture information. As shown in Table 2, various ground objects in research area present distinct features on the high-resolution GF-2 true-color imagery (B3-2-1). Pegmatite is mainly composed of quartz, feldspar, and muscovite, exhibiting an elongated and vein shape. It appearing as bright white with a high reflectivity on the imagery. The outcrop is usually small in area, often occurs as dyke swarms with a certain direction, and a ridge-like landform due to its strong resistance to weathering. Based on the satellite imagery features of various lithology units in Table 2, the spatial distribution of pegmatite with a certain scale was directly delineated through visual interpretation in Figure 5. The results suggested that a number of pegmatite dykes were distributed in the vicinity of the known Li-rich pegmatites in the ore field. They outcropped linearly in Triassic strata and Quaternary sediment around the granite pluton, showing certain metallogenic potential.

Table 2. Interpretation features of relevant ground objects in the GF-2 true color imagery.

Lithology Units	Imagery Features	Spectra	Descriptions
Granite			High overall reflectivity and increasing from blue to near infrared band; gray to bright white, blocky, large area, concentrated distribution, and clear lithology boundary.
Pegmatite			Bright white with a high reflectivity, elongated and vein shape, usually small in area, occurring as dyke swarms with a certain direction, and a ridge-like landform due to its strong resistance to weathering.
Metasediment			Blue-gray, dark tone, low overall reflectivity, large distribution area, with bedding texture.
Quaternary sediment			The reflectivity is low in visible bands, but rises sharply in near infrared band. They fan out along both sides of the river and were often covered with meadows in grassy green.

**Figure 5.** Distribution of pegmatite dykes delineated based on GF-2 imagery.

4.2. Li-Rich Pegmatite Anomaly Detection

4.2.1. MNF Transform Results

It was found that the whitening process is key to detecting small targets from hyperspectral image [83]. The MNF transform attempts to concentrate the effective information from a high-dimensional image into a lower dimensional space by maximizing the SNR and effectively reduce the noises [75]. Figure 6 shows the ZY1-02D true-color image (B29-19-10) and the false-color image (MNF3-2-1) composited by the first three components of MNF

transformation. The transformed result suggested that the differences between various lithologies have been enhanced through MNF, and presented as distinct synthesized colors in Figure 6b. The Triassic metasedimentary rocks are mainly lime green to orange depending on the degree of shading, the Quaternary sediments are aquamarine, the granites are medium blue to deep pink, and the known Li-rich pegmatites present violet red, which are visually distinguishable from the background objects. Different endmembers of ground objects were extracted based on the MNF-transformed image, and their average reflectance spectra and MNF component curves are shown in Figure 7a,b, respectively. Li-rich pegmatite differentiate from metasediments, granites and Quaternary sediments with a distinct spectrum, due to its special mineral composition and content. The research [13] suggested that the main absorption features located around ~1412 nm, ~1913 nm, and ~2205 nm and shallow secondary absorption at ~2352 nm and ~2440 nm for spodumene in pegmatite specimens. These features are probably caused by molecular water and Al-OH-bearing altered minerals (e.g., illite, montmorillonite, and kaolinite). Despite the similar spectra, Li-rich pegmatites can be distinguished from Li-poor lithologies through the distinctive reflectance magnitude, absorptions depths, the symmetry of absorption bands, and distinct key absorption wavelength [13,25]. The spectral signature of the Li-rich pegmatite acquired from the hyperspectral image is used as the reference spectrum for spectral detecting. The spectral signatures of all the pixels in the data cube are compared with the reference spectra and the best matching pixel spectra are identified as belonging to the target material.

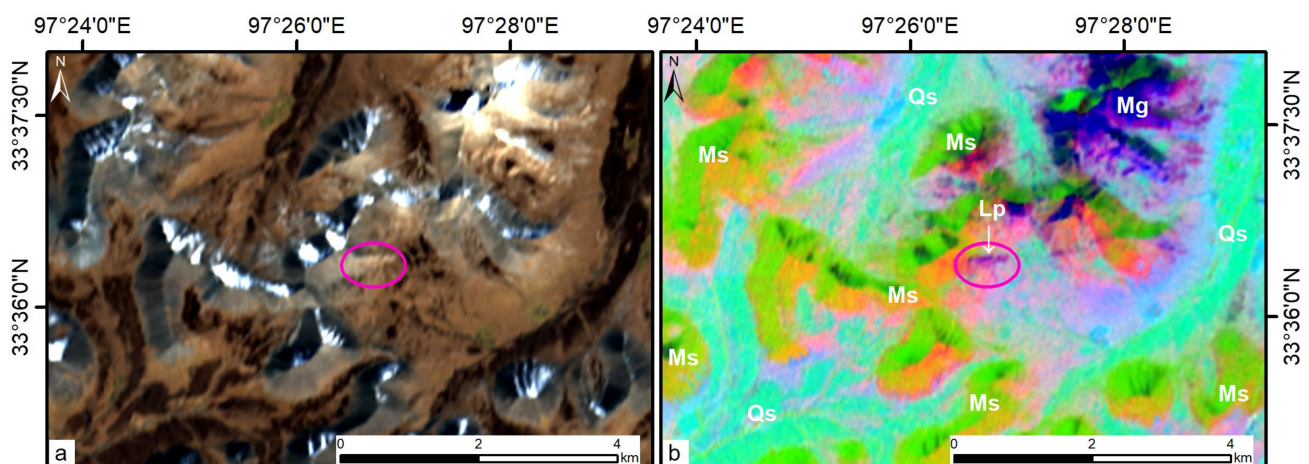


Figure 6. (a) True-color composite image (B29-19-10) and (b) MNF-transformed image (MNF3-2-1) of ZY1-02D of the study area. The purple ellipse denotes the known Li deposit area. Mg: muscovite granite, Ms: metasediment, Lp: Li-rich pegmatite, and Qs: Quaternary sediment.

4.2.2. Target Detection Results

Figure 8a–d shows the results of four algorithms, ACE, CEM, SAM, and SAMBM, respectively, for Li-rich pegmatite anomaly detection in the Zhawulong area. Hyperspectral target detection is the process of searching for a specific object on the image. Essentially, it involves the identification of spectral signatures. If the spectrum of a pixel is sufficiently similar to the reference spectrum, it can be determined that the pixel is the desired target. In the resulting grayscale images of ACE and CEM (Figure 8a,b), the pixel with a brighter level indicates a greater abundance of Li-rich pegmatites. For results of SAM and SAMBM, score value of a pixel represents the vector angle between the test spectrum and the reference spectrum, and thus a lower value indicates a better matching degree between them. To highlight the targets in bright pixels, the grayscale images were inverted for SAM and SAMBM (Figure 8c,d). The purple ellipse denotes the known Li ore field, presenting as bright pixels in all four resulting grayscale images.

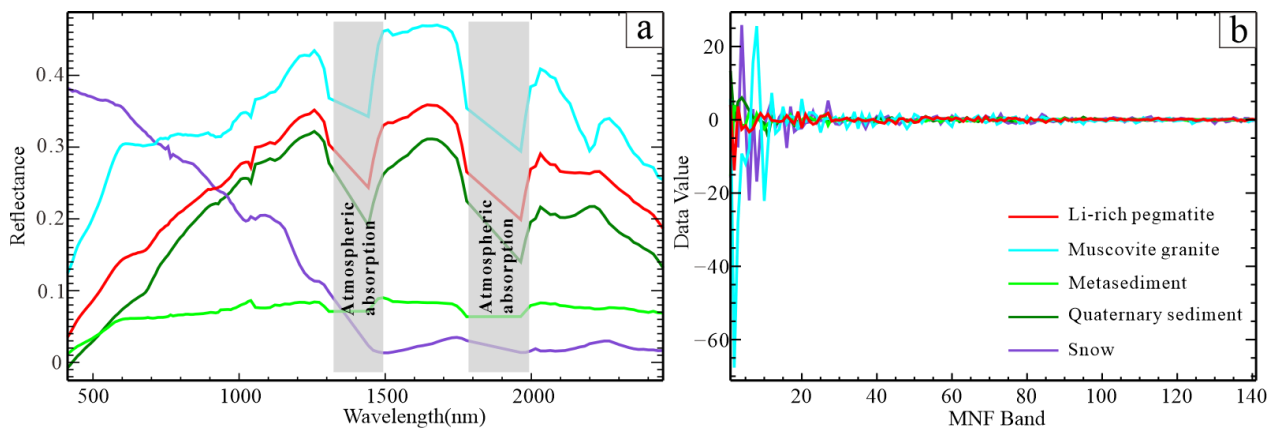


Figure 7. (a) The average reflectance spectra and (b) MNF-transformed component curves for the endmembers extracted on the ZY1-02D imagery.

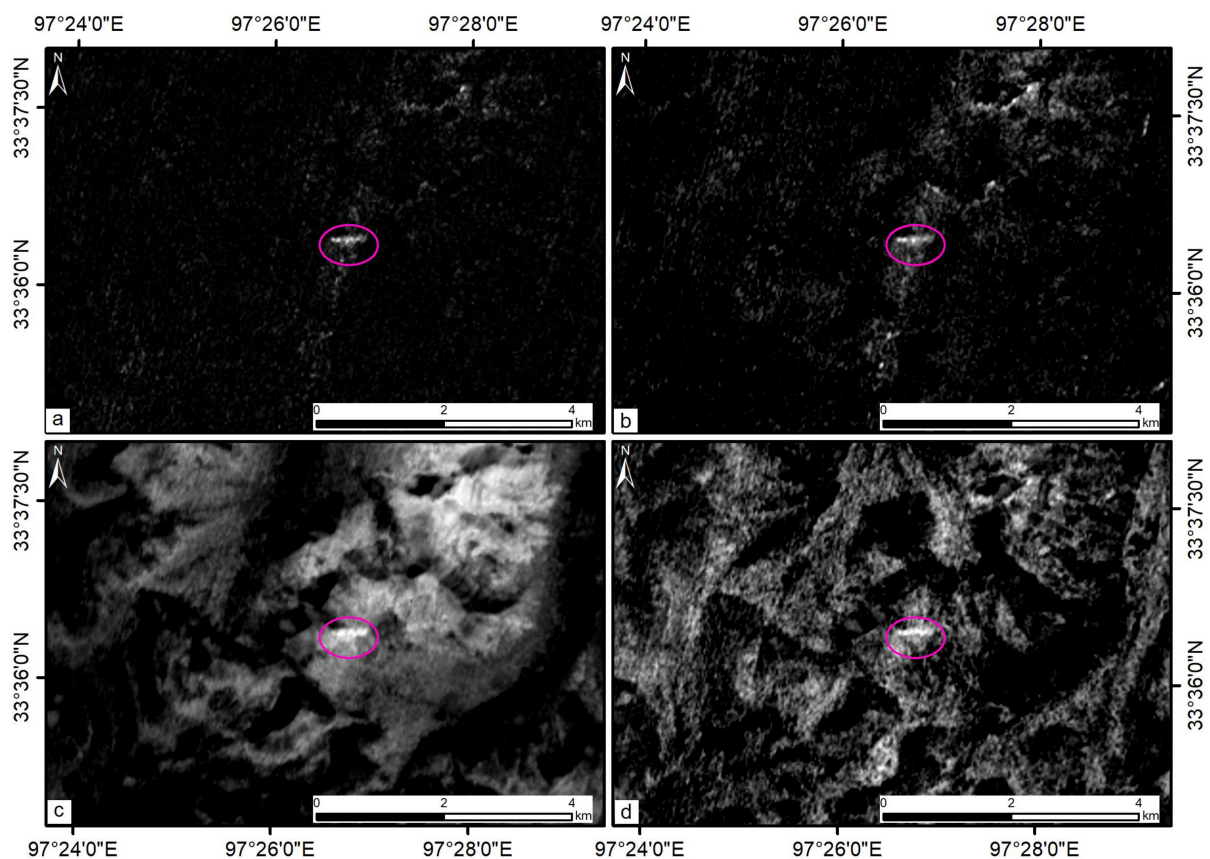


Figure 8. Li-rich pegmatite anomaly detection results of the (a) ACE, (b) CEM, (c) SAM, and (d) SAMBM algorithms applied on MNF-transformed ZY1-02D imagery. The purple ellipse denotes the known Li ore field. Brighter levels of pixels indicate higher abundances of targets.

Thresholding method was used to spatially localize the target pixels on the imagery. The thresholds were determined through inspecting the histogram of the score map. The minimum score value with prominent number of occurrences of the known Li-rich targets can be used as the lowest threshold for detecting the target region. Color density slice was also applied to the greyscale images to explicitly showcase the detection results. Consequently, the Li-rich anomaly distribution was mapped from low to high probability using a blue (low values) to red (high values) color sequence. Further, the Li-rich anomalies were superimposed with the distribution of pegmatite dykes delineated based on GF-2

high-resolution imagery (Figure 9). The results show that the known Li-rich areas exhibit high anomalies and present a zoning distribution, where the anomalies lower as farther away from the center of the ore vein. This could be attributed to the widespread presence of mixed pixels in the image caused by the low spatial resolution of spaceborne hyperspectral imaging. The central pixels of the ore body retain most of the target spectral signatures with higher pixel purity, thus showing strong target signals, i.e., high anomalies. Conversely, the closer to the edge of the ore body, the higher the proportion of pixel mixing. The mixture of target (Li-rich pegmatite) and background (metasediment, Quaternary sediment et al.) objects leads to the weakening of target spectral signatures, resulting in lower anomalies. This also demonstrates the robust reliability of various target detection techniques in extracting Li-rich pegmatites in this area. However, there are also a certain number of false anomalies due to the common existence of spectral similarity of foreign objects in nature. For example, all four algorithms incorrectly identified some granite pixels as targets to varying degrees. On the one hand, the detection results based on the partial unmixing methods (ACE and CEM) are superior to those based on the matching methods (SAM and SAMBM). On the other hand, compared with the result of SAM, it can be found that the false alarms of granite detected by the SAMBM algorithm is significantly reduced, which proves that BandMax is capable of enhancing the subtle spectral differences between background and target, thereby reducing false anomalies.

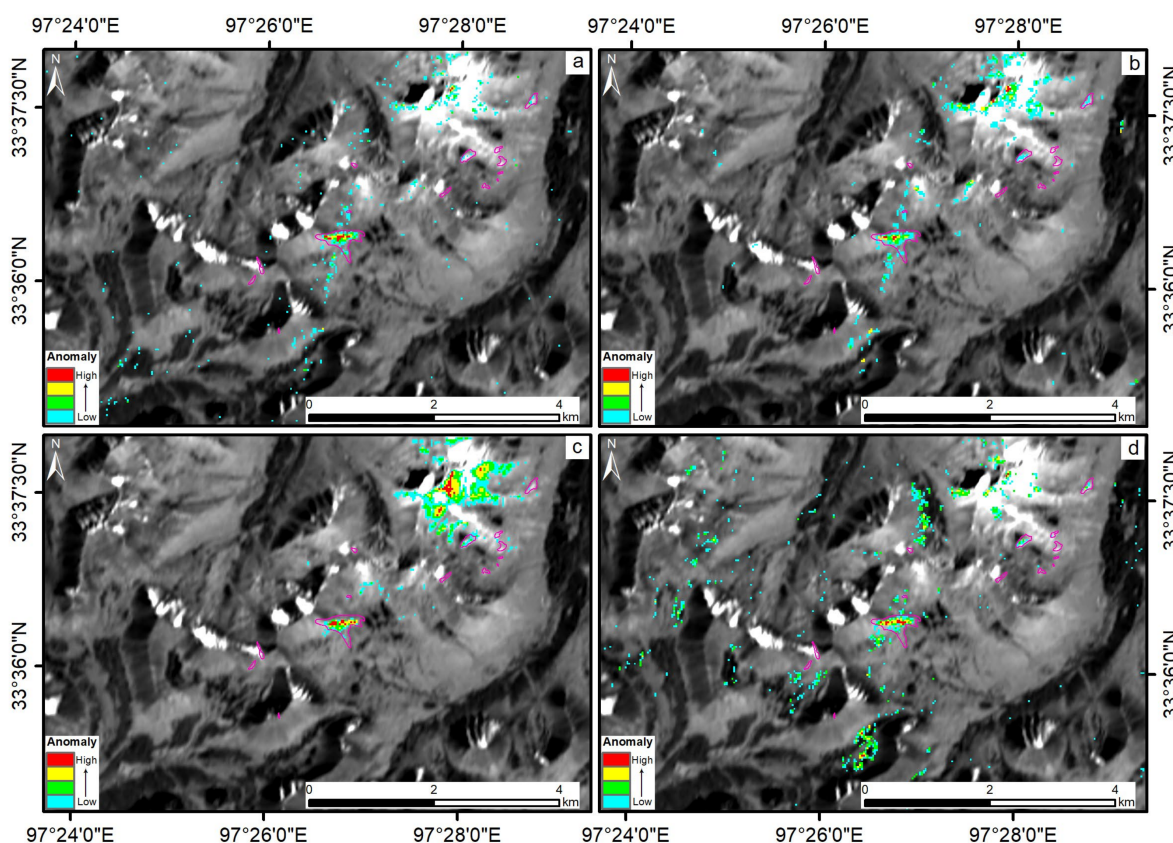


Figure 9. Density slice results of (a) ACE, (b) CEM, (c) SAM, and (d) SAMBM superimposed with the distribution of pegmatite dykes, draped over B29 greyscale image of ZY1-02D.

5. Discussion

The primary step in the exploration of hard-rock Li deposits is to identify pegmatite dykes with a certain scale. The fused GF-2 multispectral image has a spatial resolution of up to 1 m, which is benefit to quickly and accurately delineate the distribution of thin pegmatites. However, it is difficult to distinguish whether these pegmatites are mineralized due to the limited number of bands. HRS enables the acquisition of fine reflectance spectra

for minerals or rocks, allowing the identification of ground surface materials that cannot be distinguished using multispectral data [84,85]. It is even possible to determine the relative abundance and chemical composition of objects through the analysis of diagnostic spectral signatures [86]. The ZY1-02D hyperspectral image offers a spectral resolution of 10–20 nm, enabling the identification of specific minerals. However, its spatial resolution is limited to 30 m, making it susceptible to issues such as pixels mixing and spectral confusion. As a result, the false anomalies usually occurred in the detection results.

On the basis of image registration, this study overlaid the distribution of pegmatite dykes delineated using high-spatial-resolution data and the Li-rich anomalies detected through hyperspectral data to pinpoint target areas with Li mineralization potential (Figure 10). Three potential areas (A, B, C) were identified in Figure 10, where the pegmatite dykes coexisted with the distribution of Li-rich anomalies. Among these areas, A corresponds to the known Zhawulong Li ore [49,52], and the detected Li-rich anomaly distributed range agrees very well with the observed distribution of spodumene pegmatites in the field. B and C exhibited Li-rich anomalies distribution in all four algorithms, although the anomalies were relatively weak because of their small vein width. The predicted areas of B and C shared similar spectral and spatial features with the known mineralized areas (Figure 11). Therefore, they can be considered as new exploration targets and require further field verification. The X03 super-large Li-rich ore body was discovered in the deep underground of the Jiajika ore field in western Sichuan (China) through detailed investigation of the Spd-bearing pegmatite accumulation in the Quaternary covered area [87]. While the target areas of B and C are similarly exposed above the Quaternary with small surface outcrop areas, they may extend to larger volumes of dykes beneath the Quaternary cover, indicating a possibly huge potential for Li resources.

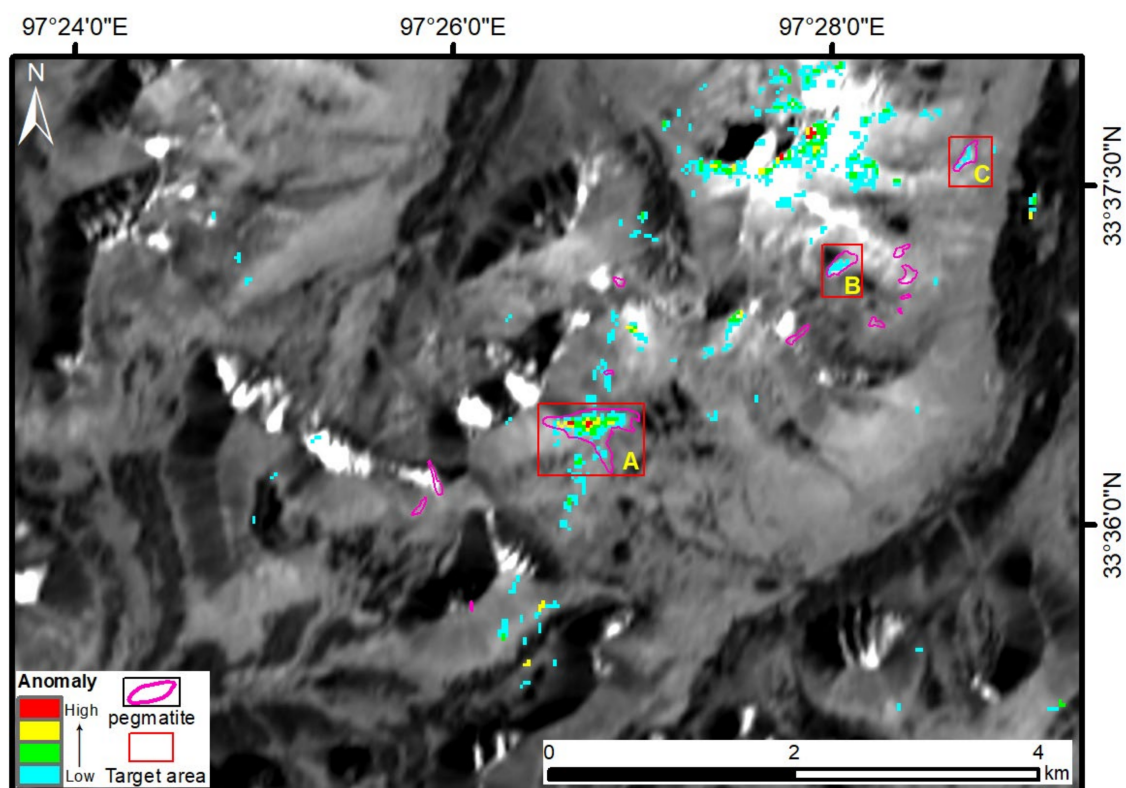


Figure 10. Prediction results of Li exploration target area integrating high-resolution (GF-2) and hyperspectral (ZY1-02D) imagery detected information. Area A denotes the known Zhawulong Li ore body [49,52], while B and C are newly discovered prospecting target areas.

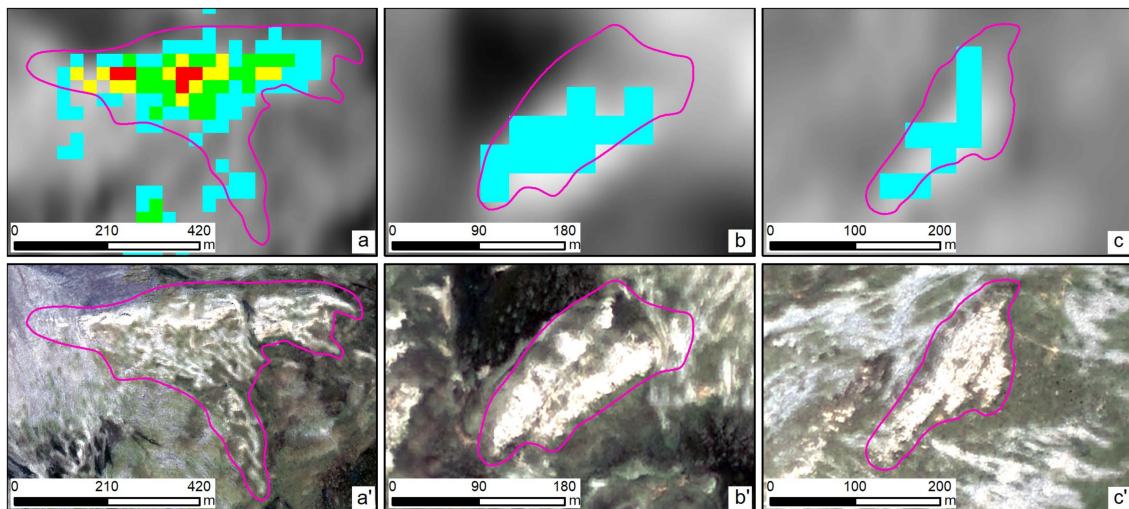


Figure 11. Comparison of detailed spectral anomalies and spatial features between (a,a') the known Li-rich pegmatite [49,52] and (b,b',c,c') the newly predicted targets.

The target detection algorithms demonstrated a high accuracy in distinguishing Li-rich pegmatites from metasediments (Figure 9). However, the challenge lies in the considerable spectral similarity and the absence of thermal infrared bands, which constrain the ability to differentiate between Li-rich pegmatites, granites, and Li-poor pegmatites. As a result, a certain number of false anomalies occur, and it is difficult to quantitatively assess their exact percentage due to the absence of a definitive training and testing dataset. Nonetheless, qualitative estimation of false anomaly occurrences can be achieved through a comparison with established geological maps and field reconnaissance. This predicament is a common challenge frequently encountered in remote sensing-based mineral exploration. Despite the mentioned limitations, the methodology can be readily applied to other regions with minimal prior knowledge, and most of the operations undertaken here can be executed using ENVI software.

The methodology proposed here for Li ore detection integrates high-resolution and hyperspectral remote sensing images, which can also be extended to explore rare metal deposits in other regions on the Tibetan Plateau. The rare metal mineralized pegmatites in the West Kunlun orogen and the HXSG orogen exhibit similar geological, geochemical, and geochronological characteristics, suggesting a common petrogenesis and metallogenesis [47,48]. They might be connected to form a giant Paleo-Tethys rare metal metallogenic belt that extends approximately 2800 km. Currently, world-class rare metal pegmatite deposits represented by the Bailongshan were discovered in the West Kunlun area [88,89], and several large-super-large rare metal deposits including Jiajika, Ke'eryin, and Zhawulong were hosted in the Songpan-Garzê area [90]. Their ore-forming ages are concentrated in the Late Triassic-Early Jurassic and they share similar metallogenic setting [47,48] (Figure 1a). However, no rare metal pegmatites have been discovered so far in the ~1200 km gap between the West Kunlun orogenic belt and the Songpan-Garzê belt (especially the Hoh-Xil region). This suggests a future target area for rare metal pegmatites exploration. Furthermore, pegmatite-type Li-Be (Beryllium) deposits were recently discovered in Qiongiagang [8] and Gabo [91] regions of the Himalayan orogen. This approves the huge potential for Li-Be mineralization in leucogranite developed areas of the Himalayan region, together with using national Li geochemical mapping [92]. These critical areas with mineralization potential are characterized by high-altitude locations with harsh environments, limited transportation access, and difficult field investigations. The method for Li detection with remote sensing technology presented in this study will serve as valuable support for future ore prospecting in these regions, especially playing a key role in early-stage exploration by narrowing down target areas and guiding the direction of mineral exploration.

Different types of materials are distinguished by their distinctive spectra, forming the theoretical foundation of HRS mapping [37]. Hence, spectral libraries play a crucial role in mineral exploration, serving as reference spectra for extracting desired minerals (e.g., Li-rich minerals). There are several spectral libraries or online databases that collect spectra of major minerals and lithologies, such as the United States Geological Survey (USGS) spectral library (<https://speclab.cr.usgs.gov/spectral-lib>, accessed on 8 August 2023) [93], ECOSTRESS spectral library (<https://speclib.jpl.nasa.gov/>, accessed on 8 August 2023) [94], and RELAB spectral database (<https://sites.brown.edu/relab/relab-spectral-database/>, accessed on 8 August 2023). However, a spectral library built exclusively dedicated to rare metal minerals and pegmatite deposits exploration is scarce [95]. Recently, a high-quality spectral library [96] of European pegmatites and related minerals has been developed in an open, ready-to-use format, which can be easily utilized by users with diverse backgrounds. The database is publicly accessible on the Zenodo platform (<https://doi.org/10.5281/zenodo.6518319>, accessed on 8 August 2023). Given the specific metallogenic conditions on the HXSG orogen [48], it is necessary to establish a spectral library exclusively focused on rare metal minerals, pegmatites, and associated wall rocks. This endeavor would be of great significance to the remote sensing-based exploration of rare metals in this region.

6. Conclusions

In this study, we integrated high-resolution and HRS data to detect the spatial distribution of Li-rich pegmatites in the ZWL area, the HXSG orogenic belt. It showed the effectiveness of target detection techniques in directly extracting anomalies associated with Li-rich pegmatite using hyperspectral satellite imagery. Based on the combined results of pegmatite delineation and Li-rich anomaly detection, this study not only accurately identified the known ZWL Li-rich deposit but also identified two additional areas with great potential for Li exploration. The procedures described here can be easily extended to other potential Li-mineralized areas without much prior knowledge, allowing the discovery of new rare metal pegmatite deposits on the Tibetan Plateau. In future research, we plan to explore multi-source data fusion techniques to overcome the limitations of spatial resolution in hyperspectral satellites, which is crucial for the exploration of rare metal pegmatites. Additionally, it is essential to investigate whether there are specific spectral parameters directly associated with Li in Li-rich minerals to reduce false alarms induced by spectral similarities with lithologies such as granite and Li-poor pegmatite. Furthermore, field validation of the predicted areas is also required when conditions permit.

Author Contributions: Conceptualization, W.D. and L.D.; methodology, W.D. and Q.L.; software, W.D.; validation, W.D., L.D. and Q.L.; formal analysis, W.D.; investigation, W.D., L.D., J.L. and L.Z.; resources, L.D. and Q.L.; data curation, W.D. and Q.L.; writing—original draft preparation, W.D.; writing—review and editing, W.D., L.D., Q.L., J.L. and L.Z.; visualization, W.D. and Q.L.; supervision, L.D. and Q.L.; project administration, L.D.; funding acquisition, L.D. All authors have read and agreed to the published version of the manuscript.

Funding: This research was funded by the Second Tibetan Plateau Scientific Expedition and Research Program (Grant No. 2019QZKK0708), the National Natural Science Foundation of China BSCTPES project (Grant No. 41988101), and the Chinese Academy of Sciences, Strategic Priority Research Program (Grant No. XDA20070301).

Data Availability Statement: The data of experimental images used to support the findings of this research are available from the corresponding author upon reasonable request.

Acknowledgments: Thanks to China Aero-Geophysical Survey and Remote Sensing Center for Natural Resources for providing GF-2 images and Aerospace Information Research Institute, Chinese Academy of Science for providing ZY1-02D data. The first author also greatly appreciates Chao Wang, Xiaoyan Xu, Lin Liu, and Fang Xu for their help in the field work.

Conflicts of Interest: The authors declare no conflict of interest.

References

1. Bradley, D.C.; Stillings, L.L.; Jaskula, B.W.; Munk, L.; McCauley, A.D. Lithium. In *Critical Mineral Resources of the United States—Economic and Environmental Geology and Prospects for Future Supply*; Schulz, K.J., DeYoung, J.J.H., Seal II, R.R., Bradley, D.C., Eds.; U.S. Geological Survey: Reston, VA, USA, 2017; pp. K1–K21. [\[CrossRef\]](#)
2. Sovacool, B.K.; Ali, S.H.; Bazilian, M.; Radley, B.; Nemery, B.; Okatz, J.; Mulvaney, D. Sustainable minerals and metals for a low-carbon future. *Science* **2020**, *367*, 30–33. [\[CrossRef\]](#) [\[PubMed\]](#)
3. Dessemond, C.; Lajoie-Leroux, F.; Soucy, G.; Laroche, N.; Magnan, J.-F. Spodumene: The Lithium Market, Resources and Processes. *Minerals* **2019**, *9*, 334. [\[CrossRef\]](#)
4. Müller, A.; Reimer, W.; Wall, F.; Williamson, B.; Menuge, J.; Brönnner, M.; Haase, C.; Brauch, K.; Pohl, C.; Lima, A.; et al. GREENPEG—Exploration for pegmatite minerals to feed the energy transition: First steps towards the Green Stone Age. *Geol. Soc. Lond. Spl. Publ.* **2023**, *526*, 193–218. [\[CrossRef\]](#)
5. Wang, H.; Huang, L.; Bai, H.; Wang, K.; Wang, Z.; Gao, H.; Zhou, J.; Qin, Y.; Wang, Y. Deposit Types, Distribution, Development and Utilization of Lithium Mineral Resources in China: Review and Perspective. *Geotecton. Metallog.* **2022**, *46*, 848–866. (In Chinese with English abstract) [\[CrossRef\]](#)
6. Groves, D.I.; Zhang, L.; Groves, I.M.; Sener, A.K. Spodumene: The key lithium mineral in giant lithium-cesium-tantalum pegmatites. *Acta Petrol. Sin.* **2022**, *38*, 1–8. [\[CrossRef\]](#)
7. Li, J.; Zou, T.; Liu, X.; Wang, D.; Ding, X. The Metallogenetic Regularities of Lithium Deposits in China. *Acta Geol. Sin.-Engl. Ed.* **2015**, *89*, 652–670. [\[CrossRef\]](#)
8. Qin, K.; Zhao, J.; He, C.; Shi, R. Discovery of the Qongjiagang giant lithium pegmatite deposit in Himalaya, Tibet, China. *Acta Petrol. Sin.* **2021**, *37*, 3277–3286. (In Chinese with English abstract) [\[CrossRef\]](#)
9. Wang, D.; Liu, S.; Li, J.; Wang, C.; Lou, D.; Yang, Y.; Li, P. New progress and trend in ten aspects of lithium exploration practice and theoretical research in China in the past decade. *J. Geomech.* **2022**, *28*, 743–764. (In Chinese with English abstract)
10. Cardoso-Fernandes, J.; Lima, A.; Roda-Robles, E.; Teodoro, A.C. Constraints and potentials of remote sensing data/techniques applied to lithium (Li)-pegmatites. *Can. Miner.* **2019**, *57*, 723–725. [\[CrossRef\]](#)
11. Cardoso-Fernandes, J.; Teodoro, A.C.; Lima, A.; Perrotta, M.; Roda-Robles, E. Detecting Lithium (Li) Mineralizations from Space: Current Research and Future Perspectives. *Appl. Sci.* **2020**, *10*, 1785. [\[CrossRef\]](#)
12. Jiang, Q.; Dai, J.; Wang, D.; Tian, S. Application of optical remote sensing to identifying granite pegmatite lithium deposits. *Miner. Depos.* **2021**, *40*, 793–804. (In Chinese with English abstract) [\[CrossRef\]](#)
13. Cardoso-Fernandes, J.; Silva, J.; Perrotta, M.M.; Lima, A.; Teodoro, A.C.; Ribeiro, M.A.; Dias, F.; Barrès, O.; Cauzid, J.; Roda-Robles, E. Interpretation of the Reflectance Spectra of Lithium (Li) Minerals and Pegmatites: A Case Study for Mineralogical and Lithological Identification in the Fregeneda-Almendra Area. *Remote Sens.* **2021**, *13*, 3688. [\[CrossRef\]](#)
14. Cardoso-Fernandes, J.; Teodoro, A.C.; Lima, A. Remote sensing data in lithium (Li) exploration: A new approach for the detection of Li-bearing pegmatites. *Int. J. Appl. Earth Obs. Geoinf.* **2019**, *76*, 10–25. [\[CrossRef\]](#)
15. Cardoso-Fernandes, J.; Teodoro, A.C.; Lima, A.; Roda-Robles, E. Semi-Automatization of Support Vector Machines to Map Lithium (Li) Bearing Pegmatites. *Remote Sens.* **2020**, *12*, 2319. [\[CrossRef\]](#)
16. Köhler, M.; Hanelli, D.; Schaefer, S.; Barth, A.; Knobloch, A.; Hielscher, P.; Cardoso-Fernandes, J.; Lima, A.; Teodoro, A.C. Lithium Potential Mapping Using Artificial Neural Networks: A Case Study from Central Portugal. *Minerals* **2021**, *11*, 1046. [\[CrossRef\]](#)
17. Teodoro, A.C.; Santos, D.; Cardoso-Fernandes, J.; Lima, A.; Brönnner, M. Identification of pegmatite bodies, at a province scale, using machine learning algorithms: Preliminary results. In Proceedings of the SPIE Remote Sensing, Online Only, 13–18 September 2021; p. 1186308. [\[CrossRef\]](#)
18. Peng, G.; Ye, Z.; Gao, G.; Feng, D.; Xiong, Y. Pegmatite remote sensing extraction and metallogenetic prediction in Azubai area, Xinjiang. *Trans. Nonferr. Met. Soc. China* **2011**, *21*, s543–s548. [\[CrossRef\]](#)
19. Peng, G.; Gao, G. Remote sensing prospecting of pegmatite deposits in the azubai region, xinjiang. *Geotecton. Metallog.* **2013**, *37*, 109–117. (In Chinese with English abstract) [\[CrossRef\]](#)
20. Dai, J.; Wang, D.; Dai, H.; Liu, L.; Wu, Y. Geological mapping and ore-prospecting study using remote sensing technology in Jiajika area of Western Sichuan Province. *Geol. China* **2017**, *44*, 389–398. (In Chinese with English abstract)
21. Fan, Y.; Wang, H.; Yang, X.; Peng, Q.; Qin, X.; Yang, J.; Zhang, S.; Tan, F. Application of high-resolution remote sensing technology to the prospecting for rare metal mineralization belt. *Remote Sens. Nat. Resour.* **2018**, *30*, 128–134, (In Chinese with English abstract).
22. Gao, Y.; Bagas, L.; Li, K.; Jin, M.; Liu, Y.; Teng, J. Newly Discovered Triassic Lithium Deposits in the Dahongliutan Area, North West China: A Case Study for the Detection of Lithium-Bearing Pegmatite Deposits in Rugged Terrains Using Remote-Sensing Data and Images. *Front. Earth Sci.* **2020**, *8*, 591966. [\[CrossRef\]](#)
23. Yao, F.; Xu, X.; Yang, J. A technology for identifying Li-Be pegmatite using Aster remote sensing data in granite of Gobi shallow-covered area: A case study of recognition and prediction of Li-Be pegmatite in Jingerquan, Xinjiang. *Miner. Depos.* **2020**, *39*, 686–696. (In Chinese with English abstract) [\[CrossRef\]](#)
24. Jiang, Q.; Dai, J.; Wang, D.; Wang, C.; Tian, S. Lithium-bearing Pegmatite Exploration in Western Altun, Xinjiang, using Remote-Sensing Technology. *Acta Geol. Sin.-Engl. Ed.* **2023**, *97*, 681–694. [\[CrossRef\]](#)
25. Chen, L.; Zhang, N.; Zhao, T.; Zhang, H.; Chang, J.; Tao, J.; Chi, Y. Lithium-Bearing Pegmatite Identification, Based on Spectral Analysis and Machine Learning: A Case Study of the Dahongliutan Area, NW China. *Remote Sens.* **2023**, *15*, 493. [\[CrossRef\]](#)

26. Gao, Y.; Chen, C.; Ma, H.; Li, S.; Qiu, L.; Wang, C.; Wang, L. Identification and prediction of lithium bearing pegmatite dikes in Dahongliutan ore concentration area in West Kunlun, Xinjiang. *Miner. Depos.* **2023**, *42*, 41–54. (In Chinese with English abstract) [[CrossRef](#)]
27. Mashkoo, R.; Ahmadi, H.; Rahmani, A.B.; Pekkan, E. Detecting Li-Bearing Pegmatites Using Geospatial Technology: The Case of SW Konar Province, Eastern Afghanistan. *Geocarto Int.* **2022**, *37*, 14105–14126. [[CrossRef](#)]
28. Gemusse, U.; Lima, A.; Teodoro, A. Pegmatite spectral behavior considering ASTER and Landsat 8 OLI data in Naipa and Muiane mines (Alto Ligonha, Mozambique). In Proceedings of the SPIE Remote Sensing, Berlin, Germany, 10–13 September 2018; p. 107901L. [[CrossRef](#)]
29. Gemusse, U.; Lima, A.; Teodoro, A. Comparing different techniques of satellite imagery classification to mineral mapping pegmatite of Muiane and Naipa: Mozambique. In Proceedings of the SPIE Remote Sensing, Strasbourg, France, 9–12 September 2019; p. 111561E. [[CrossRef](#)]
30. Arvelyna, Y.; Shuichi, M.; Atsushi, M.; Nguno, A.; Mhopjeni, K.; Muyongo, A.; Sibeso, M.; Muvangua, E. Hyperspectral mapping for rock and alteration mineral with Spectral Angle Mapping and Neural Network classification method: Study case in Warmbad district, south of Namibia. In Proceedings of the 2011 IEEE International Geoscience and Remote Sensing Symposium, Vancouver, BC, Canada, 24–29 July 2011; pp. 1752–1754. [[CrossRef](#)]
31. Booyesen, R.; Lorenz, S.; Thiele, S.T.; Fuchsloch, W.C.; Marais, T.; Nex, P.A.M.; Gloaguen, R. Accurate hyperspectral imaging of mineralised outcrops: An example from lithium-bearing pegmatites at Uis, Namibia. *Remote Sens. Environ.* **2022**, *269*, 112790. [[CrossRef](#)]
32. Momose, A.; Miyatake, S.; Arvelyna, Y.; Nguno, A.; Mhopjeni, K.; Sibeso, M.; Muyongo, A.; Muvangua, E. Mapping pegmatite using HyMap data in southern Namibia. In Proceedings of the 2011 IEEE International Geoscience and Remote Sensing Symposium, Vancouver, BC, Canada, 24–29 July 2011; pp. 2216–2217. [[CrossRef](#)]
33. Oshigami, S.; Yamaguchi, Y.; Uezato, T.; Momose, A.; Arvelyna, Y.; Kawakami, Y.; Yajima, T.; Miyatake, S.; Nguno, A. Mineralogical mapping of southern Namibia by application of continuum-removal MSAM method to the HyMap data. *Int. J. Remote Sens.* **2013**, *34*, 5282–5295. [[CrossRef](#)]
34. Santos, D.; Teodoro, A.; Lima, A.; Cardoso-Fernandes, J. Remote sensing techniques to detect areas with potential for lithium exploration in Minas Gerais, Brazil. In Proceedings of the SPIE Remote Sensing, Strasbourg, France, 9–12 September 2019; p. 111561F. [[CrossRef](#)]
35. Cardoso-Fernandes, J.; Teodoro, A.C.; Lima, A.; Menuge, J.; Brönnner, M.; Steiner, R. Sentinel-1 and ALOS data for lineament extraction: A comparative study. In Proceedings of the SPIE Remote Sensing, Berlin, Germany, 5–8 September 2022; p. 122680X. [[CrossRef](#)]
36. Shirmard, H.; Farahbakhsh, E.; Müller, R.D.; Chandra, R. A review of machine learning in processing remote sensing data for mineral exploration. *Remote Sens. Environ.* **2022**, *268*, 112750. [[CrossRef](#)]
37. Clark, R.N.; King, T.V.; Klejwa, M.; Swayze, G.A.; Vergo, N. High spectral resolution reflectance spectroscopy of minerals. *J. Geophys. Res.* **1990**, *95*, 12653–12680. [[CrossRef](#)]
38. Bedini, E. The use of hyperspectral remote sensing for mineral exploration: A review. *J. Hyperspectr. Remote Sens.* **2017**, *7*, 189–211. [[CrossRef](#)]
39. Ding, W.; Ding, L. Hyperspectral remote sensing of rock and mineral and its application prospects on the Tibetan Plateau. *Chin. J. Geol.* **2022**, *57*, 924–944. (In Chinese with English abstract)
40. Dong, X.; Gan, F.; Li, N.; Zhang, S.; Li, T. Mineral mapping in the Duolong porphyry and epithermal ore district, Tibet, using the Gaofen-5 satellite hyperspectral remote sensing data. *Ore Geol. Rev.* **2022**, *151*, 105222. [[CrossRef](#)]
41. Nie, S.; Yin, A.; Rowley, D.B.; Jin, Y. Exhumation of the Dabie Shan ultra-high-pressure rocks and accumulation of the Songpan-Ganzi flysch sequence, central China. *Geology* **1994**, *22*, 999–1002. [[CrossRef](#)]
42. Pullen, A.; Kapp, P.; Gehrels, G.E.; Vervoort, J.D.; Ding, L. Triassic continental subduction in central Tibet and Mediterranean-style closure of the Paleo-Tethys Ocean. *Geology* **2008**, *36*, 351–354. [[CrossRef](#)]
43. Ding, L.; Yang, D.; Cai, F.L.; Pullen, A.; Kapp, P.; Gehrels, G.E.; Zhang, L.Y.; Zhang, Q.H.; Lai, Q.Z.; Yue, Y.H.; et al. Provenance analysis of the Mesozoic Hoh-Xil-Songpan-Ganzi turbidites in northern Tibet: Implications for the tectonic evolution of the eastern Paleo-Tethys Ocean. *Tectonics* **2013**, *32*, 34–48. [[CrossRef](#)]
44. Zhang, L.-Y.; Ding, L.; Pullen, A.; Xu, Q.; Liu, D.-L.; Cai, F.-L.; Yue, Y.-H.; Lai, Q.-Z.; Shi, R.-D.; Ducea, M.N.; et al. Age and geochemistry of western Hoh-Xil-Songpan-Ganzi granitoids, northern Tibet: Implications for the Mesozoic closure of the Paleo-Tethys ocean. *Lithos* **2014**, *190–191*, 328–348. [[CrossRef](#)]
45. Xu, Z.; Fu, X.; Zhao, Z.; Li, G.; Zheng, Y.; Ma, Z. Discussion on relationships of Gneiss Dome and Metallogenic regularity of Pegmatite-Type lithium deposits. *Earth Sci.* **2019**, *44*, 1452–1463. (In Chinese with English abstract)
46. Xu, Z.; Wang, R.; Zhao, Z.; Fu, X. On the structural backgrounds of the large-scale “hard-rock type” lithium ore belts in China. *Acta Geol. Sin.* **2018**, *92*, 1091–1106. (In Chinese with English abstract)
47. Li, P.; Li, J.; Chou, I.-M.; Wang, D.; Xiong, X. Mineralization Epochs of Granitic Rare-Metal Pegmatite Deposits in the Songpan-Ganzê Orogenic Belt and Their Implications for Orogeny. *Minerals* **2019**, *9*, 280. [[CrossRef](#)]
48. Yan, Q.; Wang, H.; Chi, G.; Wang, Q.; Hu, H.; Zhou, K.; Zhang, X. Recognition of a 600-KM-LONG Late Triassic Rare Metal (Li-Rb-Be-Nb-Ta) Pegmatite Belt in the Western Kunlun Orogenic Belt, Western China. *Econ. Geol.* **2022**, *117*, 213–236. [[CrossRef](#)]

49. Li, X.; Li, J.; Liu, Y.; Xiong, C. Geochemical features of muscovite granite in the Zhawulong granitic pegmatite type rare metal deposit, western Sichuan. *Geol. Rev.* **2018**, *64*, 231–242. (In Chinese with English abstract) [[CrossRef](#)]
50. Li, X. Metallogenic Mechanism of Zhawulong Granitic Pegmatite-Type Lithium Deposit in Western Sichuan. Master's Thesis, Chinese Academy of Geological Science, Beijing, China, 2019. (In Chinese with English abstract)
51. Xiong, X.; Li, J.; Wang, D.; Li, S.; Lin, H. Fluid Characteristics and Evolution of the Zhawulong Granitic Pegmatite Lithium Deposit in the Ganzi-Songpan Region, Southwestern China. *Acta Geol. Sin.-Engl. Ed.* **2019**, *93*, 943–954. [[CrossRef](#)]
52. Yan, Q.; Li, J.; Li, X.; Liu, Y.; Li, P.; Xiong, X. Source of the Zhawulong granitic pegmatite-type lithium deposit in the Songpan-Ganzê orogenic belt, Western Sichuan, China: Constrants from Sr-Nd-Hf isotopes and petrochemistry. *Lithos* **2020**, *378–379*, 105828. [[CrossRef](#)]
53. Yang, R.; Hao, X.; Peng, Y. A comprehensive study on geology and geophysics of Zhawulong lithium deposit. *Miner. Depos.* **2021**, *40*, 842–856. (In Chinese with English abstract) [[CrossRef](#)]
54. Bai, Z.; Lin, H.; Li, S.; Chen, B.; Bai, J.; Fu, J.; Jin, T. Characteristics and genesis analysis of pegmatite type lithium-polymetallic deposit in the Caolong area of the northern segment of the Sanjiang belt, Qinghai. *J. Qinghai Univ.* **2018**, *36*, 86–93. (In Chinese with English abstract)
55. Li, W.; Li, S.; Wang, B.; Wang, C.; Liu, J.; Zhang, X.; Cao, J.; Xu, C.; Liu, J.; Jin, T. Discovery of the (beryl-bearing) spodumene pegmatite in the Caolong area in the Sanjiang Northern section of the Qinghai: Implications for Li-Be mineralization. *Geotecton. Metallog.* **2021**; *in press*. (In Chinese with English abstract) [[CrossRef](#)]
56. Li, W.; Liu, J.; Li, S.; Jia, C.; Wang, C.; Zhou, J.; Wang, C.; Xu, C.; Tan, S.; Hu, J.; et al. Discovery and Mineralization Significance of Early Jurassic (Beryl- and Lepidolite-) Spodumene-bearing Pegmatites in the Gaduo-Zaduo Area of the Yushu Region, Northeastern Tibet. *Geotecton. Metallog.* **2022**, *46*, 924–950. (In Chinese with English abstract) [[CrossRef](#)]
57. Liu, J.-H.; Wang, Q.; Xu, C.-B.; Zhou, J.-S.; Wang, B.-Z.; Li, W.-F.; Li, S.-P.; Huang, T.-Y.; Yan, Q.-H.; Song, T.-Z.; et al. Geochronology of the Chakabeishan Li-(Be) rare-element pegmatite, Zongwulong orogenic belt, northwest China: Constraints from columbite-tantalite U-Pb and muscovite-lepidolite $40\text{Ar}/39\text{Ar}$ dating. *Ore Geol. Rev.* **2022**, *146*, 104930. [[CrossRef](#)]
58. Huang, W.; Sun, S.; Jiang, H.; Gao, C.; Zong, X. GF-2 Satellite 1m/4m Camera Design and In-Orbit Commissioning. *Chin. J. Electron.* **2018**, *27*, 1316–1321. [[CrossRef](#)]
59. Liang, S.; Wei, H.; Gan, F.; Chen, L.; Xiao, C. Preliminary application evaluation of GF-2 satellite data in remote sensing geological survey. *Spacecr. Recovery Remote Sens.* **2015**, *36*, 63–72. (In Chinese with English abstract)
60. Yuan, K.; Li, X.; Liu, R.; Zhang, L.; Zhang, Q.; Cao, Z.; Wang, Y. Mapping bare rock in open-pit limestone mining area using Gaofen-2 satellite image. *Earth Sci.* **2022**; *in press*. (In Chinese with English abstract)
61. Zhang, L.; Na, X.; Liu, Z.; Zang, S. Remote Sensing Geological Interpretation Based on Domestic GF-2 Satellite Imagery: A Case Study of the Awulale Area. *Geol. Sci. Technol. Inf.* **2018**, *37*, 233–240. (In Chinese with English abstract) [[CrossRef](#)]
62. Sun, W.; Chen, B.; Messinger, D. Nearest-neighbor diffusion-based pan-sharpening algorithm for spectral images. *Opt. Eng.* **2014**, *53*, 013107. [[CrossRef](#)]
63. Liu, Y.; Sun, D.; Han, B.; Zhu, H.; Liu, S.; Yuan, J. Development of advanced visible and short-wave infrared hyperspectral imager onboard ZY-1-02D satellite. *Spacecr. Eng.* **2020**, *29*, 85–92. (In Chinese with English abstract)
64. Niu, C.; Tan, K.; Wang, X.; Han, B.; Ge, S.; Du, P.; Wang, F. Radiometric Cross-Calibration of the ZY1-02D Hyperspectral Imager Using the GF-5 AHSI Imager. *IEEE Trans. Geosci. Remote Sens.* **2022**, *60*, 5519612. [[CrossRef](#)]
65. Shang, K.; Xiao, C.; Gan, F.; Wei, H.; Wang, C. Estimation of soil copper content in mining area using ZY1-02D satellite hyperspectral data. *J. Appl. Remote Sens.* **2021**, *15*, 042607. [[CrossRef](#)]
66. Yu, J.; Zhang, L.; Li, Q.; Li, Y.; Huang, W.; Sun, Z.; Ma, Y.; He, P. 3D autoencoder algorithm for lithological mapping using ZY-1 02D hyperspectral imagery: A case study of Liuyuan region. *J. Appl. Remote Sens.* **2021**, *15*, 042610. [[CrossRef](#)]
67. Li, G.; Yang, X.; Zhang, X.; Li, X.; Li, D.; Du, C. Application and analysis of ZY1-02D hyperspectral data in geological and mineral survey. *Remote Sens. Nat. Resour.* **2021**, *33*, 134–140. (In Chinese with English abstract)
68. Sun, Y.; Liu, J.; Zhai, D.; Liu, Z.; Zhang, F.; Zhao, Y.; Liu, P.; Wang, Z. Alteration minerals mapping and identification of gold mineralization belt based on ZY1-02D hyperspectral data in the Toudiaoquan-Nandatan area, Gansu Province. *Geol. Explor.* **2022**, *58*, 399–409. (In Chinese with English abstract) [[CrossRef](#)]
69. Zhao, Z.; Zhang, X.; Chen, Q.; Zhang, R.; Li, W.; Cao, X. Mapping of alteration minerals and prospecting potential analysis of Pulang porphyry copper deposit: Evidence from remote sensing data of Ziyuan-1 02D satellite. *Sediment. Geol. Tethyan Geol.* **2022**, *42*, 17–29. (In Chinese with English abstract)
70. Zhang, B. Advancement of hyperspectral image processing and information extraction. *J. Remote Sens.* **2016**, *20*, 1062–1090. (In Chinese with English abstract) [[CrossRef](#)]
71. Farrand, W.H.; Harsanyi, J.C. Mapping the distribution of mine tailings in the Coeur d'Alene River Valley, Idaho, through the use of a constrained energy minimization technique. *Remote Sens. Environ.* **1997**, *59*, 64–76. [[CrossRef](#)]
72. Pour, A.B.; Hashim, M.; Hong, J.K.; Park, Y. Lithological and alteration mineral mapping in poorly exposed lithologies using Landsat-8 and ASTER satellite data: North-eastern Graham Land, Antarctic Peninsula. *Ore Geol. Rev.* **2019**, *108*, 112–133. [[CrossRef](#)]

73. Zhang, X.; Pazner, M.; Duke, N. Lithologic and mineral information extraction for gold exploration using ASTER data in the south Chocolate Mountains (California). *ISPRS J. Photogramm. Remote Sens.* **2007**, *62*, 271–282. [[CrossRef](#)]
74. Du, B.; Zhang, L.; Li, P.; Zhong, Y. A constrained energy minimization method in sub-pixel target detection based on minimization noise fraction. *J. Image Graph.* **2009**, *1*, 1850–1857. (In Chinese with English abstract)
75. Green, A.A.; Berman, M.; Switzer, P.; Craig, M.D. A transformation for ordering multispectral data in terms of image quality with implications for noise removal. *IEEE Trans. Geosci. Remote Sens.* **1988**, *26*, 65–74. [[CrossRef](#)]
76. Manolakis, D.G.; Marden, D.; Shaw, G.A. Hyperspectral Image Processing for Automatic Target Detection Applications. *Linc. Lab. J.* **2003**, *14*, 79–116.
77. Bedini, E.; Chen, J. Application of PRISMA satellite hyperspectral imagery to mineral alteration mapping at Cuprite, Nevada, USA. *J. Hyperspectr. Remote Sens.* **2020**, *10*, 87–94. [[CrossRef](#)]
78. Li, Q.; Wei, X.; Zhang, B.; Yan, S.; Liu, X. The spectral analysis and information extraction for small geological target detection using hyperion image. In Proceedings of the International Conference on Earth Observation Data Processing and Analysis, Wuhan, China, 28–30 December 2008; p. 72850N. [[CrossRef](#)]
79. Kruse, F.A.; Lefkoff, A.B.; Boardman, J.W.; Heidebrecht, K.B.; Shapiro, A.T.; Barloon, P.J.; Goetz, A.F.H. The spectral image processing system (SIPS)—Interactive visualization and analysis of imaging spectrometer data. *Remote Sens. Environ.* **1993**, *44*, 145–163. [[CrossRef](#)]
80. Galileo Group, Inc. BandMaxTM—Hyperspectral Target Detection Utility. Available online: <http://www.galileo-gp.com/bandmax%20-%20hyperspectral%20detection%20utility%20-%20galileo%20group,%20inc.%20-%20summer%202003.pdf> (accessed on 12 June 2023).
81. Kumar, H.; Sharma, R.N.; Krishna, A.P. Application of Advanced Remote Sensing Data in Mineral Exploration in the Vicinity of Heavy Dense Forest Cover Area of Jharkhand and Odisha State Mining Area. *Int. J. Environ. Ecol. Eng.* **2020**, *14*, 243–246. [[CrossRef](#)]
82. Wang, Z.; Hu, G. Alteration/minerals information extraction from EO-1 Hyperion data. In Proceedings of the Geoinformatics 2006: GNSS and Integrated Geospatial Applications, Wuhan, China, 28–29 October 2006; p. 64190A. [[CrossRef](#)]
83. Geng, X.; Zhao, Y. Principle of small target detection for hyperspectral imagery. *Sci. China Ser. D Earth Sci.* **2007**, *50*, 1225–1231. [[CrossRef](#)]
84. Meer, F.D.v.d.; van der Werff, H.M.A.; van Ruitenbeek, F.J.A.; Hecker, C.A.; Bakker, W.H.; Noomen, M.F.; van der Meijde, M.; Carranza, E.J.M.; Smeth, J.B.d.; Woldai, T. Multi- and hyperspectral geologic remote sensing: A review. *Int. J. Appl. Earth Obs. Geoinf.* **2012**, *14*, 112–128. [[CrossRef](#)]
85. Ramakrishnan, D.; Bharti, R. Hyperspectral remote sensing and geological applications. *Curr. Sci.* **2015**, *108*, 879–891.
86. Van der Meer, F.; Kopačková, V.; Koucká, L.; van der Werff, H.M.A.; van Ruitenbeek, F.J.A.; Bakker, W.H. Wavelength feature mapping as a proxy to mineral chemistry for investigating geologic systems: An example from the Rodalquilar epithermal system. *Int. J. Appl. Earth Obs. Geoinf.* **2018**, *64*, 237–248. [[CrossRef](#)]
87. Fu, X.; Yuan, L.; Wang, D.; Hou, L.; Pan, M.; Hao, X.; Liang, B.; Tang, Y. Mineralization characteristics and prospecting model of newly discovered X03 rare metal vein in Jiajika orefield, Sichuan. *Miner. Depos.* **2015**, *34*, 1172–1186. (In Chinese with English abstract) [[CrossRef](#)]
88. Wang, H.; Gao, H.; Zhang, X.-Y.; Yan, Q.-H.; Xu, Y.; Zhou, K.; Dong, R.; Li, P. Geology and geochronology of the super-large Bailongshan Li-Rb-(Be) rare-metal pegmatite deposit, West Kunlun orogenic belt, NW China. *Lithos* **2020**, *360–361*, 105449. [[CrossRef](#)]
89. Wang, H.; Li, P.; Ma, H.; Zhu, B.; Qiu, L.; Zhang, X.; Dong, R.; Zhou, K.; Wang, M.; Wang, Q. Discovery of the Bailongshan superlarge lithium-rubidium deposit in Karakorum, Hetian, Xinjiang, and its prospecting implication. *Geotecton. Metallog.* **2017**, *41*, 1053–1062. (In Chinese with English abstract) [[CrossRef](#)]
90. Li, J. Mineralizing Mechanism and Continental Geodynamics of Typical Pegmatite Deposits in Western Sichuan, China. Ph.D. Dissertation, China University of Geosciences (Beijing), Beijing, China, 2006. (In Chinese with English abstract)
91. Li, G.; Fu, J.; Guo, W.; Zhang, H.; Zhang, L.; Dong, S.; Li, Y.; Wu, J.; Jiao, Y.; Jin, C. Discovery of the Gabo granitic pegmatitetype lithium deposit in the Kulagangri Dome, eastern Himalayan metallogenic belt, and its prospecting implication. *Acta Petrol. Mineral.* **2022**, *41*, 1109–1119. (In Chinese with English abstract)
92. Wang, X.; Liu, H.; Wei, W.; Zhou, J.; Zhang, B.; Xu, S. Geochemical abundance and spatial distribution of lithium in China: Implications for potential prospects. *Acta Geosci. Sin.* **2020**, *41*, 797–806. (In Chinese with English abstract)
93. Kokaly, R.F.; Clark, R.N.; Swayze, G.A.; Livo, K.E.; Hoefen, T.M.; Pearson, N.C.; Wise, R.A.; Benzel, W.M.; Lowers, H.A.; Driscoll, R.L.; et al. *USGS Spectral Library Version 7; Data Series 1035*; U.S. Geological Survey: Reston, VA, USA, 2017; p. 61. [[CrossRef](#)]
94. Meerdink, S.K.; Hook, S.J.; Roberts, D.A.; Abbott, E.A. The ECOSTRESS spectral library version 1.0. *Remote Sens. Environ.* **2019**, *230*, 111196. [[CrossRef](#)]

95. Cardoso-Fernandes, J.; Dias, F.; Lima, A.; Teodoro, A.; Odile, B.; Cauzid, J.; Perrotta, M.; Roda-Robles, E.; Ribeiro, M. Tools for Remote Exploration: A Lithium (Li) Dedicated Spectral Library of the Fregeneda-Almendra Aplite-Pegmatite Field. *Data* **2021**, *6*, 33. [[CrossRef](#)]
96. Cardoso-Fernandes, J.; Santos, D.; Rodrigues de Almeida, C.; Lima, A.; Teodoro, A.C.; GREENPEG Project Team. Spectral Library of European Pegmatites, Pegmatite Minerals and Pegmatite Host-Rocks—The GREENPEG project database. *Earth Syst. Sci. Data* **2023**, *15*, 3111–3129. [[CrossRef](#)]

Disclaimer/Publisher’s Note: The statements, opinions and data contained in all publications are solely those of the individual author(s) and contributor(s) and not of MDPI and/or the editor(s). MDPI and/or the editor(s) disclaim responsibility for any injury to people or property resulting from any ideas, methods, instructions or products referred to in the content.